Monthly Notices of the ROYAL ASTRONOMICAL SOCIETY
MNRAS **451,** 2462–2478 (2015) doi:10.1093/mnras/stv1111

IRAS 19135+3937: an SRd variable as interacting binary surrounded by a circumbinary disc

N. Gorlova,[1⋆] H. Van Winckel,[1⋆] N. P. Ikonnikova,[2] M. A. Burlak,[2] G. V. Komissarova,[2] A. Jorissen,[3] C. Gielen,[4] J. Debosscher[1] and P. Degroote[1]

[1]*Instituut voor Sterrenkunde, Katholieke Universiteit Leuven, Celestijnenlaan 200D, B-3001 Leuven, Belgium*
[2]*Lomonosov Moscow State University, Sternberg Astronomical Institute, 13 Universitetskij prospekt, 119234 Moscow, Russia*
[3]*Institut d'Astronomie et d'Astrophysique, Université Libre de Bruxelles, CP 226, Boulevard du Triomphe, B-1050 Bruxelles, Belgium*
[4]*Belgian Institute for Space Aeronomy, B-1180 Brussels, Belgium*

Accepted 2015 May 14. Received 2015 May 13; in original form 2014 September 28

ABSTRACT

Semi-regular (SR) variables are not a homogeneous class and their variability is often explained due to pulsations and/or binarity. This study focuses on IRAS 19135+3937, an SRd variable with an infrared excess indicative of a dusty disc. A time series of high-resolution spectra, *UBV* photometry as well as a very accurate light curve obtained by the *Kepler* satellite, allowed us to study the object in unprecedented detail. We discovered it to be a binary with a period of 127 d. The primary has a low surface gravity and an atmosphere depleted in refractory elements. This combination of properties unambiguously places IRAS 19135+3937 in the subclass of post-asymptotic giant branch stars with dusty discs. We show that the light variations in this object cannot be due to pulsations, but are likely caused by the obscuration of the primary by the circumbinary disc during orbital motion. Furthermore, we argue that the double-peaked Fe emission lines provide evidence for the existence of a gaseous circumbinary Keplerian disc inside the dusty disc. A secondary set of absorption lines has been detected near light minimum, which we attribute to the reflected spectrum of the primary on the disc wall, which segregates due to the different Doppler shift. This corroborates the recent finding that reflection in the optical by this type of discs is very efficient. The system also shows a variable Hα profile indicating a collimated outflow originating around the companion. IRAS 19135+3937 thus encompasses all the major emergent trends about evolved disc systems, that will eventually help to place these objects in the evolutionary context.

Key words: stars: AGB and post-AGB – binaries: spectroscopic – circumstellar matter – stars: variables: general.

1 INTRODUCTION

There are four types of semi-regular (SR) variables, each designated alphabetically from a to d. IRAS 19135+3937 belongs to the last category, 'd'. SRd variables represent a poorly understood group of warm (spectral types F–K) giants and supergiants. Their light curves exhibit variations on the time-scales 30–1100 d, that are only quasi-regular and lack characteristic features of the radial pulsators with similar periods, such as Cepheids and RV Tau stars. There is, however, one intriguing feature in the behaviour of some RV Tau stars that is reminiscent of the SR variability. Normally RV Tau stars pulsate with periods between 30 and 150 d, with two alternating minima per cycle, shallow and deep. An 'RV Tau b' subgroup, however, shows an additional variability in the mean magnitude, amplitude, or relative strengths of the minima. This additional 'secondary period' variability occurs on the time-scale that overlaps with variability in the SRd-s with long periods. This phenomenon is referred to as 'long secondary periods' (LSPs), and the origin of LSPs is still a matter of debate (e.g. Wood et al. 1999; Kiss et al. 2007). The two major hypotheses discussed in the literature are variable obscuration (Lloyd Evans 1974; Fokin 1994; Pollard et al. 1997) and an interplay between various pulsation modes (Buchler & Kovacs 1987).

Modelling of the better studied Galactic systems is hindered by the lack of direct distance measurements, hence luminosities. In terms of kinematics, chemical composition, and emission line strength there appears to be no systematic difference between SRd-s and RV Tau stars (Wahlgren 1993). Chemical composition studies

⋆E-mail: n27032001@yahoo.com (NG); Hans.VanWinckel@ster.kuleuven.be (HVW)

indicate that both groups are heterogeneous and include halo, as well as disc objects (Giridhar, Lambert & Gonzalez 2000; Britavskiy et al. 2012). Based on the rarity, presence of the circumstellar matter, and the luminosities deduced for the Magellanic Clouds objects, most of these objects must represent late evolutionary stages of low-mass stars, being either post-red giant or post-asymptotic giant branch (pAGB) stars (Wallerstein 2002; Van Winckel 2003; Kamath, Wood & Van Winckel 2014). Since there is no evidence that SRd-s and RV Tau stars would represent different stellar populations or different evolutionary stages, the reason for the SR behaviour must be sought in the properties of individual systems.

Binarity could be such a property, but how exactly would it cause the observed light variations? Mutual eclipses of the companions can be ruled out, as the fraction of systems with an edge-on orientation or where both companions are evolved giants, must be negligible. Furthermore, the SR character requires that the eclipsing body should be variable. It has long been known that many RV Tau stars have near-infrared excesses, indicating presence of hot dust up to the sublimation temperatures (Evans 1985). The modelling of the spectral energy distribution (SED; Gielen et al. 2009), as well as interferometric measurements (Deroo et al. 2007; Hillen et al. 2013) have demonstrated that the dust resides in a disc. The discs have typical inner radii of only a few astronomical units (∼10 stellar radii, $R_\star$) and inner walls of substantial scaleheight.

At the same time, there is a growing evidence from the radial velocity (RV) studies that evolved objects with discs are all binaries (Van Winckel et al. 1999, 2009). Based on the deduced orbits for the visible giant primaries, the discs must be circumbinary. The variability can then be naturally explained by the obscuration of the primary star by the inner rim of the disc, as the line of sight to the star probes different heights above the disc plane along its orbit (Waelkens & Waters 1993). The cycle-to-cycle irregularities could be caused by inhomogeneity or precession of the disc.

To test this theory, one has to find a correlation between the SR behaviour, the shape of the SED, and binarity. In reality, it is not always possible to prove binarity based on RV variations alone, for example in case of small inclination angle or strong pulsations. In 2009, we started to monitor a number of RV Tau, SR, W Vir, and chemically peculiar pAGB stars with the echelle spectrograph HERMES (Van Winckel et al. 2010; Gorlova et al. 2011). Besides detecting RV variations consistent with binarity and obtaining orbital solutions for some systems, in many of them we also discovered specific phase-dependent Hα profiles (Gorlova et al. 2012b, 2013; Van Winckel et al. 2012). Normally these profiles are P Cyg-like or have a double-peak emission, but only during the superior conjunction of the pAGB primary they were found to develop strong blue-shifted absorption. Witt et al. (2009), based on the observations of a similar phenomenon in the central star of the Red Rectangle (RR) nebula, explained the Hα line-profile variability by a model in which a jet is powered by accretion from the giant primary to the invisible (likely a main-sequence, MS) companion. IRAS 19135+3937, originally included in our sample due to the disc-like infrared (IR) excess, turned out to be one of such objects. Besides Hα, it caught our eye also because of the rather smooth light-curve with a large amplitude, which is not typical for long-period pulsators. IRAS 19135+3937 thus presented a good case for testing binary theory for SR variables.

The variability of IRAS 19135+3937 has been first discovered by amateur astronomers (Sallman & Droege 2004), who determined a period $P = 125.4$ d and an amplitude $\Delta V = 0.9$ mag. Based on these observations, the star was included in the General Catalogue of Variable Stars as an SRd variable V677 Lyr (Kazarovets et al. 2013). The star was also observed in the course of the All Sky Automated Survey (ASAS), where it was classified as a 'QPER' type, which is an SR variable with a stable period (128.8 d; Pigulski et al. 2009). The star is relatively faint ($V \sim 11$ mag) and had not been discussed in the literature when we started its observations. Recently, Rao & Giridhar (2014) performed an abundance analysis and found it to be a moderately metal-poor star ([Fe/H] $= -1$ dex) with some peculiarities.

In Gorlova, Van Winckel & Jorissen (2012a), we presented the first RV curve of IRAS 19135+3937 that revealed its binarity. We also showed a number of peculiar spectral lines including Hα, and pointed to the similarity with BD+46°442, the first object discovered in our survey to display this type of Hα line profile variability (Gorlova et al. 2012b). Since then we have tripled the number of observed spectra of IRAS 19135+3937 and followed up with multiband photometry. Here, we provide a comprehensive analysis of these data in order to understand the cause of the SR variability in this object. We deduce strong observational constraints on the geometry of the system and study the ongoing interaction processes.

2 NEW OBSERVATIONS AND DATA REDUCTION

2.1 Photometry

We observed IRAS 19135+3937 with a photoelectric *UBV*-photometer (Lyutyj 1971) attached to the 60-cm telescope Zeiss-1 (located in Crimea) of the Sternberg Astronomical Institute (SAI, Russia). The diameter of the photometer diaphragm was set to 27 arcsec. 74 measurements have been made between 2012 and 2013, which overlaps with the epoch of our spectroscopic observations.

To obtain colour terms for the transformation of the instrumental *ubv* system to the standard Johnson's *UBV* one, we observed standard stars in NGC 6633 (Mermilliod 1986). By solving equations $\Delta V = \Delta v - k_1\Delta(b - v)$, $\Delta(B - V) = k_2\Delta(b - v)$, and $\Delta(U - B) = k_3\Delta(u - b)$, we obtained the following colour terms: $k_1 = 0.082 \pm 0.010$, $k_2 = 0.980 \pm 0.010$, $k_3 = 1.081 \pm 0.015$. We used HD 179909 as a comparison star, with the following magnitudes adopted from Mermilliod (1991):[1] $V = 8.285 \pm 0.015$, $B - V = -0.070 \pm 0.010$, $U - B = -0.330 \pm 0.010$. The typical accuracy of our absolute photometry is of the order of 0.01 mag.

The measurements are given in Table A1. The observations revealed sinusoidal-like variations in brightness and colour, with a period consistent with earlier reports.

2.2 Spectroscopy

We collected 61 spectra of IRAS 19135+3937 with the HERMES fibre echelle spectrograph mounted on the 1.2-m telescope Mercator on La Palma (Raskin et al. 2011). The observations were carried out in the years 2009–2013, with an average cadence of one observation per two weeks. The exposure time varied with the brightness of the star and the weather conditions, being on average 1400 s. A typical signal-to-noise ratio (S/N) in the central orders (around Hα) was ∼35, which was needed for obtaining a cross-correlation function (CCF) suitable for the RV determination (Section 5.1). All spectra in our survey have been collected using the high-resolution fibre configuration, that provides $R \sim 80\,000$ and a wavelength coverage

[1] VizieR online catalogue II/168 'Homogeneous Means in the UBV System'.

between 3800 and 9000 Å, and reduced with a dedicated PYTHON-based pipeline HERMESDRS.

The pipeline provides science graded output. A quick-look of the extracted spectrum is available during the actual observations, and the full reduction is automatically performed after sunrise. The pipeline first averages in 2D biases, arcs, and flat-fields. The cross-order profile with the two slices is modelled on a daily basis and used at extraction, during which the cosmic clipping is also performed. We do not use optimal extraction. The read-out noise is typically 3–4 electrons. Sky subtraction is not performed, because all spatial information is lost due to the scrambling properties of the optical fibre. The contamination by the interstellar emission, however, is not a concern for our evolved stars, that are located away from star-forming regions.

The stability of the zero-point of our arc-based wavelength calibration is monitored with the help of the International Astronomical Union RV standards. Over five years of HERMES operation, we obtain a standard deviation of 0.080 km s^{-1} based on 2329 measurements of different RV standards, measured as a spread over the mean of every standard. The shifts are mainly cased by the pressure variations during the night (Raskin et al. 2011). More details on the instrument and data reduction can be found at the HERMES webpage[2] and in Gorlova et al. (2012b).

3 BASIC PROPERTIES

3.1 Photospheric parameters and chemical composition

For the chemical abundance study, we used an average of three well-exposed consecutive spectra obtained on 2009 June 29, with maximum S/N $\sim$ 150 near 6000 Å in the combined spectrum. These observations were carried out near maximum light, and metallic lines were nearly symmetric and easy to measure. As will be shown in Section 5.1, this phase corresponds to the superior conjunction of the pAGB primary, when its obscuration by the circumstellar disc and the contribution from a putative companion should be minimal.

We followed the same procedure for the physical parameters and abundance determination as for another similar object BD+46°442, as described in Gorlova (2011) and Gorlova et al. (2012b). Briefly, to get the initial estimate of the effective temperature ($T_{\rm eff}$) and surface gravity ($\log g$), we matched the observed profiles of H δ, H γ, and H β (wings only) with the pre-computed state of the art model profiles of Coelho et al. (2005), and Paschen 14 with those of Munari & Castelli (2000). The two distinct sets of model spectra had to be employed in order to cover both Balmer and Paschen series. After visual inspection, we selected the following best combinations of $T_{\rm eff}$/$\log g$:[3] 6000/1.0 $\pm$ 0.5, 6250/2.0, and 5750/0.5.

At the next stage of iteration, we examined the correlation of the Fe abundance obtained from the Fe I and Fe II lines with their equivalent widths (EWs). The abundances (for Fe, as well as other elements) were computed from the EWs using MOOG10, which is the latest version of the local thermodynamic equilibrium (LTE) abundance determination code by Sneden (1973), and the ATLAS9 model

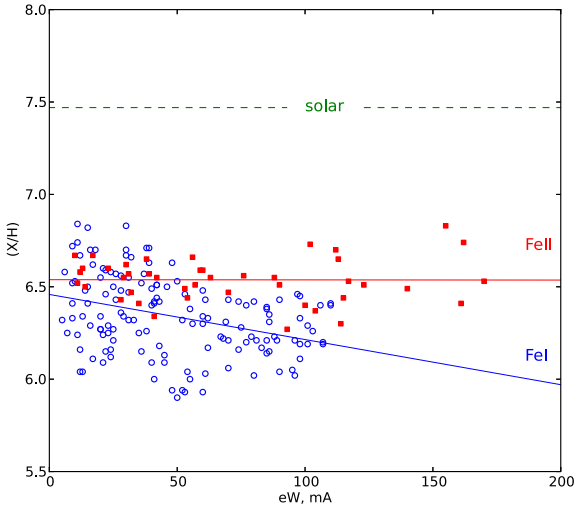

Figure 1. Ionization balance for Fe lines, that was used to derive the following atmospheric parameters for IRAS 19135+3937: $V_{\rm tur}$ = 5 km s^{-1}, $\log g$ = 1.0, $\log \epsilon$(Fe) = 6.50. The plot is shown for $T_{\rm eff}$ = 6000 K, which is the best-fitting value from the fit to the hydrogen lines. Straight lines designate linear fits to the data.

atmospheres of R. Kurucz in the updated version of Castelli & Kurucz (2003). We started with models with the solar metallicity, but re-computed the final abundances with $[M/{\rm H}] = -1.0$ to better match the deduced overall metal deficiency of IRAS 19135+3937. The EWs in the observed spectrum were measured using our PYTHON-based program, which includes a module to disentangle close line pairs. The latter is important for IRAS 19135+3937, because the lines are relatively broad (FWHM = 12.5 km s^{-1} in the considered phase). To maximize the number of measured lines, we also augmented our previous atomic line list (which was an updated version from Kovtyukh & Andrievsky 1999), with two others: a list previously used by the Leuven group (Van Winckel & Reyniers 2000), which is largely based on the solar list by Thévenin (1989, 1990), and a SPECTROWEB[4] list, as compiled and improved by Lobel (2008, 2011). Where the oscillator strengths ($\log gf$) for the same line differed between the lists by more than 0.25 dex, the value was used that provided an abundance best matching the rest of the lines of the same ion.

To study the Fe I/Fe II balance, the Fe abundance was computed with MOOG10 for three best values of $T_{\rm eff}$ (5750, 6000, and 6250 K), a range of $\log g$ =0.5–3.0 with a step of 0.5 dex, and a range of microturbulences $V_{\rm tur}$ = 3–8 km s^{-1} with a step of 1 km s^{-1}. Only Fe I lines with EW$\leq$110 mÅ and Fe II lines with EW$\leq$200 mÅ were retained for further analysis, as they lie on the linear part of the curve of growth. For each model, the derived abundances from the individual lines have been plotted against the EWs. We obtained different values for the microturbulence when trying to remove the abundance trends with EWs for the neutral and ionic transitions. As discussed in Gorlova et al. (2012b), at these temperatures and gravities strong Fe I lines are susceptible to deviations from LTE, therefore, $V_{\rm tur}$ from the Fe II lines was adopted. The surface gravity is then established by requiring that the average Fe abundance from the Fe II lines matches the extrapolated to EW = 0 abundance from the Fe I lines (Fig. 1). Following this procedure for each of the three values of $T_{\rm eff}$ obtained from the hydrogen line analysis, we obtained

[2] http://www.mercator.iac.es/instruments/hermes/

[3] The following units are used throughout the paper: K for the effective temperature $T_{\rm eff}$, dex[cm s^{-2}] for the logarithm of surface gravity $\log g$, km s^{-1} for the microturbulent velocity $V_{\rm tur}$, and dex for the logarithm of the elemental abundance with respect to the hydrogen abundance (using designation (X/H) for $\log \epsilon$(X) on the scale where $\log \epsilon$(H) = 12, and [X/H] when expressing difference with the Sun: [X/H] = (X/H)$-$(X/H)$_\odot$).

[4] http://spectra.freeshell.org/spectroweb.html

the following $T_{\rm eff}$/log g/$V_{\rm tur}$/[Fe/H] solutions: 6000/1.0/5.0/−0.97 (best model), 6250/1.5/6.0/−0.84, and 5750/0.5/5.0/−1.12, where the Fe abundance is expressed relative to the solar value of 7.47 in the scale log ϵ(H) = 12.

Similar rules were used for the rest of the elements to combine abundances from the individual lines: for ions the abundances of all lines with EW ≤ 200 mÅ were averaged; for neutrals an extrapolation to EW = 0 was performed for lines with EW ≤ 110 mÅ when possible, otherwise, abundances of lines with EW ≤ 50 mÅ were averaged, or, if such lines did not exist (Co I, Zn I), lines with EW up to 110 mÅ have been averaged. These final abundances for the best atmospheric model are given in Table 1, along with the difference with abundances obtained using two other closest models.

All elements in IRAS 19135+3937 show sub-solar abundance, ranging from −0.5 for the CNO group to −1.5 for some heavy elements. The underabundance appears to correlate with the condensation temperature of the element, as shown in Fig. 2. This is a common phenomenon in pAGB disc systems. It is explained by contamination of the photosphere by the re-processed gas from the disc. The gas is poor in refractory elements because they condensed into grains. Rao & Giridhar (2014) carried an independent analysis of the IRAS 19135+3937 composition, in the framework of their survey of objects occupying the RV Tau box on the *IRAS* colour–colour diagram. The spectrum that they investigated was obtained in the phase of line doubling, and so is less favourable for measuring EWs than ours. Nevertheless, they obtained very similar atmospheric parameters including metallicity: $T_{\rm eff}$/log g/$V_{\rm tur}$/[Fe/H] = 6000/0.5/4.1/−1.04. The depletion pattern that we find for this star is relatively weak, so it is not surprising that Rao & Giridhar (2014) did not manage to detect it. They did point out the deficiency of the α-elements Ca and Ti, that have a higher condensation temperature than Fe, but were reluctant to ascribe it to the depletion effect due to a lack of a stronger Sc deficiency and of the Zn enrichment. Our values for these elements are more consistent with the depletion pattern, except for Zn, but the latter is only represented by 1 or 2 lines in both studies.

Table 1. Chemical composition of IRAS 19135+3937.

Z	Ion	log ϵ	[X/H]	rms	Δ[X/H]		N	Flag
					A	B		
6	C I	8.10	−0.42	0.11	−0.03	+0.03	8	2
7	N I	7.76	−0.17	0.11	+0.03	−0.05	4	2
8	O I	8.21	−0.68	0.21	−0.09	+0.09	2	3
11	Na I	5.72	−0.60	–	−0.08	+0.08	1	3
12	Mg I	6.88	−0.70	–	−0.05	+0.03	1	3
13	Al I	5.60	−0.87	0.10	−0.05	+0.04	2	3
14	Si I	7.06	−0.48	0.12	−0.07	+0.07	13	2
14	Si II	7.26	−0.36	–	−0.01	−0.09	1	3
16	S I	6.57	−0.55	0.11	−0.09	+0.09	2	3
20	Ca I	5.20	−1.16	0.17	−0.11	+0.09	12	2
21	Sc II	1.93	−1.22	0.14	−0.26	+0.22	11	1
22	Ti I	3.77	−1.24	0.01	−0.21	+0.19	2	3
22	Ti II	3.81	−1.20	0.12	−0.24	+0.19	24	1
23	V II	3.17	−0.80	–	−0.22	+0.19	1	3
24	Cr I	4.68	−0.93	0.12	−0.11	+0.11	8	2
24	Cr II	4.63	−0.96	0.07	−0.16	+0.13	13	1
25	Mn I	4.38	−1.0	–	−0.14	+0.13	1	3
26	Fe I	6.46	−1.01	0.20	−0.13	+0.13	142	2
26	Fe II	6.54	−0.94	0.12	−0.18	+0.14	43	1
27	Co I	3.77	−1.12	–	−0.12	+0.12	1	3
28	Ni I	5.35	−0.88	0.14	−0.13	+0.14	27	2
29	Cu I	2.83	−1.38	–	−0.2	+0.2	1	3
30	Zn I	3.55	−1.02	–	−0.15	+0.15	1	3
39	Y II	0.66	−1.56	0.11	−0.26	+0.25	6	1
40	Zr II	1.45	−1.13	–	−0.24	+0.25	1	3
56	Ba II	0.92	−1.21	–	−0.3	+0.26	1	3
57	La II	0.17	−1.02	–	−0.3	+0.3	1	3
58	Ce II	0.33	−1.20	0.04	−0.29	+0.29	3	1
60	Nd II	0.46	−1.10	0.11	−0.31	+0.32	4	1
62	Sm II	−0.04	−1.03	0.07	−0.31	+0.32	2	3
63	Eu II	−0.49	−0.99	0.06	−0.26	+0.27	2	3

Note. Column [X/H] gives abundances for the best-fitting model $T_{\rm eff}$/log g/$V_{\rm tur}$ = 6000/1.0/5.0, while the Δ[X/H] column shows the response of the abundances to the change in the adopted $T_{\rm eff}$, with cases A and B corresponding to the models 5750/0.5/5.0 and 6250/1.5/6.0. The flags in the last column have been introduced as follows: (1) – most reliable abundances, for ions where three and more lines with EW≤200 mÅ were available for averaging; (2) – less reliable abundances, obtained for neutrals by extrapolating to EW = 0 the abundances from lines with EW≤110 mÅ, or if not possible, by averaging lines with EW≤50 mÅ; (3) – least reliable abundances, obtained by averaging less than three lines with EW≤200 mA and EW≤110 mÅ for ions and neutrals, respectively. The number of used lines is indicated in the last but one column. The rms column marks the mean deviation either from the average value or from the interpolated line.

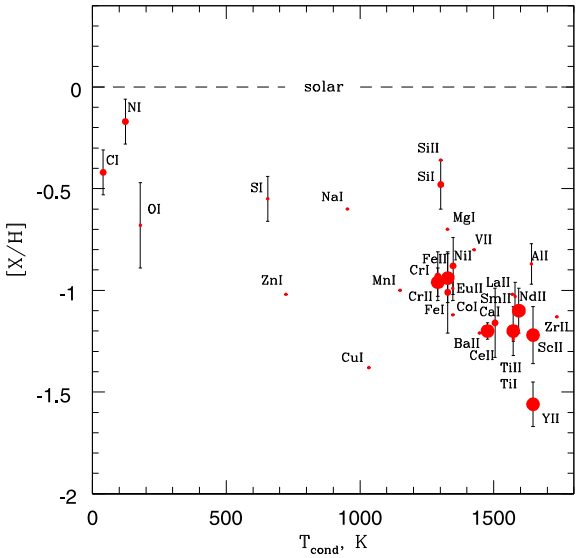

Figure 2. Abundances of IRAS 19135+3937 (computed with the best-fitting model $T_{\rm eff}$/log g/$V_{\rm tur}$ = 6000/1.0/5.0) versus condensation temperature. The error bars represent the line-to-line scatter, while the circle size designates the reliability flag: the larger the circle, the more reliable the flag.

The range of temperatures and gravities obtained for IRAS 19135+3937 near maximum light allows us to estimate its spectral type (SpT). Kovtyukh (2007) adapted the traditional method of the SpT determination, that rests on the relative strengths of certain lines, to the echelle spectra of FGK supergiants. The S/N of our spectrum is not sufficient to apply this method directly, but we can use a tabulated SpT–$T_{\rm eff}$ relationship from that study to estimate the range of SpTs for IRAS 19135+3937 based on its $T_{\rm eff}$: F6 (6268 K)–F9 (5752 K). In addition, we searched the UVES Paranal Observatory Project (UVES POP) archive[5] (Bagnulo et al. 2003) for bright field stars with spectral classification adopted from Buscombe & Foster (1995), that would be similar to IRAS 19135+3937. Given the peculiar abundance pattern of IRAS 19135+3937 and a wide range of line widths exhibited by supergiants, we did not intend to find

[5] http://www.eso.org/sci/observing/tools/uvespop.html

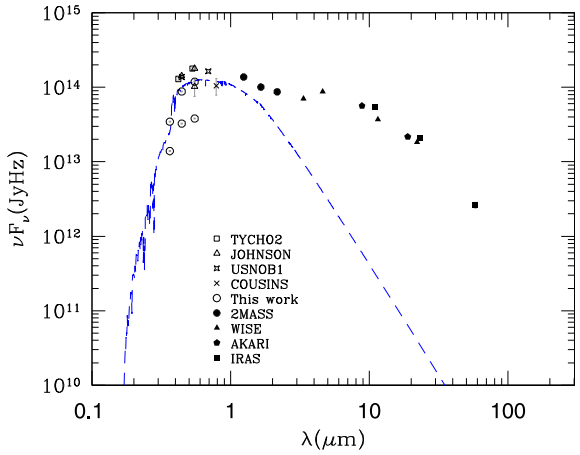

Figure 3. SED based on our photometry and the measurements from the VizieR data base. Dashed line: Kurucz photospheric model with our spectroscopically determined parameters $T_{\rm eff}/\log g/[M/{\rm H}] = 6000/1.0/-1.0$, reddened by $E(B-V) = 0.18$, and shifted to match $V_{\rm max}$ of our epoch of observations.

a precisely matching standard, but rather wanted to independently verify SpT of IRAS 19135+3937 implied by its $T_{\rm eff}$. The spectrum of HD 108968 (F7Ib/II) appeared to be the closest match to our spectrum of IRAS 19135+3937, hence we adopted SpT F7±2 I/II for the latter.

3.2 IR excess

The SED of IRAS 19135+3937 is shown in Fig. 3. Besides our measurements shown for the maximum and minimum light, we also plot photometry from the VizieR data base. In particular, the measurements in the Johnson's *B* and *V* pass-bands originate from the 'All-sky compiled catalogue of 2.5 million stars' (Kharchenko & Roeser 2009). Another measurement in the Johnson *V*, and a measurement in the Cousin's *I* pass-band originate from the 'The Amateur Sky Survey (TASS) Mark IV patches photometric catalog, version 2' (Droege et al. 2006). The rest of the data points arise from the annotated ground and space-based missions. The scatter in the optical is due to the variability of the source.

Using the photospheric parameters determined in Section 3.1, we can estimate the stellar contribution in the SED and identify any flux excess. The photospheric contribution in Fig. 3 is represented by a Kurucz model (Castelli & Kurucz 2003) with $T_{\rm eff} = 6000$ K, $\log g = 1.0$, $[M/{\rm H}] = -1.0$, and $V_{\rm tur} = 2.0$. The model was reddened by $E(B-V) = 0.18$, which was deduced from the comparison of the observed $B-V$ colour in the maximum light with the expected colour for an F7 supergiant (Section 4). We used reddening law of Cardelli, Clayton & Mathis (1989) with $A_V/E(B-V) = 3.1$ with modification of O'Donnell (1994) in the optical to NIR regime. It is clear that IRAS 19135+3937 has a strong IR excess. The SED is typical for pAGB stars with dusty discs, where the excess usually starts at 2 μm, peaks at around 10 μm and drops with a blackbody slope towards the far-IR, indicating the presence of large grains (De Ruyter et al. 2005).

4 PHOTOMETRIC VARIABILITY

In Fig. 4, we show our light and colour curves of IRAS 19135+3937, that are clearly variable. The variations in all three

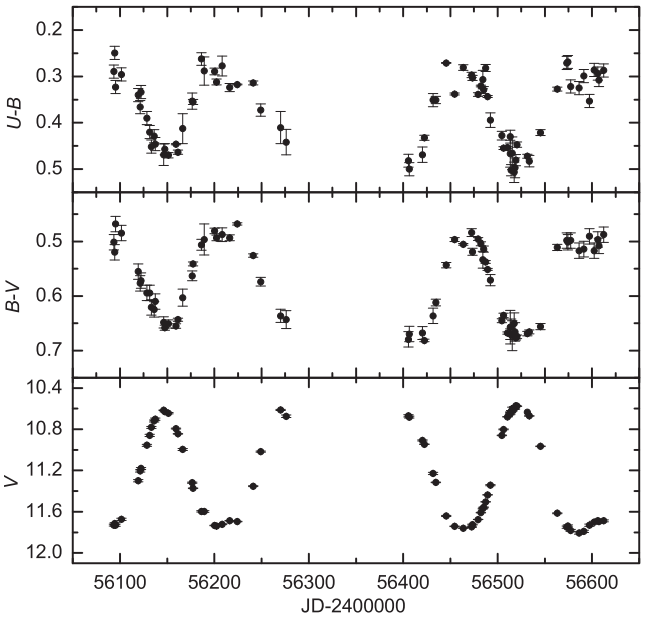

Figure 4. *V*-band light, and $U-B$, $B-V$ colour curves for IRAS 19135+3937 using our photometry from 2012–2013.

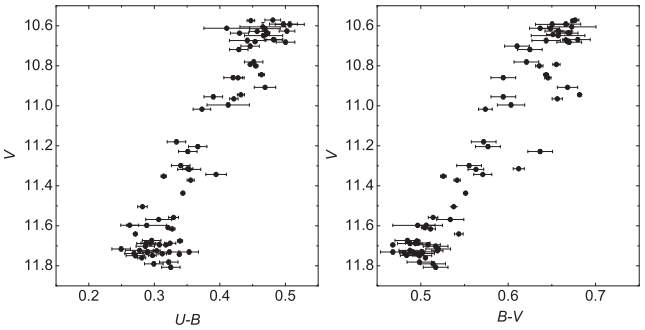

Figure 5. $U-B$ and $B-V$ colour variations with the *V*-band magnitude for IRAS 19135+3937 in 2012–2013.

bands are periodic and occur in phase. Using the PERIOD04[6] program of Lenz & Breger (2005), that relies on the discrete Fourier transform for period determination, we obtained $P = 126.53 \pm 0.40$ d for all three pass-bands. The peak-to-peak amplitude increases with wavelength: $\Delta U = 1.0$ mag, $\Delta B = 1.1$ mag, $\Delta V = 1.2$ mag. The average magnitudes in 2012–2013 were: $<U> = 12.17$ mag, $<B> = 11.80$ mag, $<V> = 11.23$ mag. The relationship between brightness and colour is striking (Fig. 5): *when the star fades, it gets bluer*. Clearly, this behaviour cannot be explained simply by variations in the extinction, as it would produce the opposite effect.

To verify how IRAS 19135+3937 behaved in the past, we searched for time series photometry in the publicly available catalogues. In 1989–1992 it was observed by *Hipparcos*. In *Tycho-2* (Høg et al. 2000) it has the designation TYC 3125−2395−1. 180 measurements are given, as well as the mean magnitudes $\langle B_T \rangle = 10.886$ and $\langle V_T \rangle = 10.200$. Converting to the Johnson system using the transformation of Bessell (2000), we obtain: $\langle B \rangle = 10.75$ mag and $\langle V \rangle = 10.13$ mag. The errors of the

[6] http://www.univie.ac.at/tops/Period04/

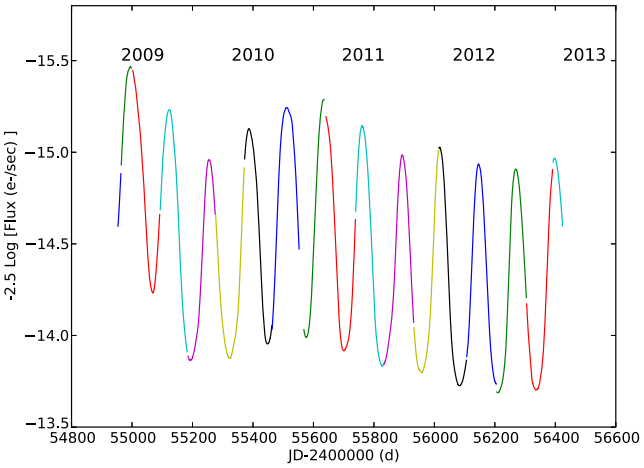

Figure 6. *Kepler* light curve. Colours mark separate acquisition sequences.

Tycho measurements, however, are too large ($\sigma_{V_T} = 0.29$ mag and $\sigma_{B_T} = 0.32$ mag) for a reliable period determination.

In 2003–2004 IRAS 19135+3937 was monitored by TASS. 46 measurements in Johnson-Cousins V and I_C pass-bands for the first time revealed variability of the star (Sallman & Droege 2004). We obtained the following values of the period for this data set: 127.11 ± 0.95 d (V band) and 127.11 ± 0.71 d (I_C band). According to these observations, the $V - I_C$ colour did not exhibit sinusoidal variations with amplitudes larger than the uncertainties of the photometric observations (± 0.07 mag), in contrast to the pronounced $U - B$ and $B - V$ colour variations observed by us in 2012–2013.

Between 2006 May and 2008 January IRAS 19135+3937 was observed by ASAS. The measurements are given in 'The catalogue of variable stars in the Kepler field of view'.[7] The source with a designation 191512+3942.8 has a period $P = 128.8$ d, mean magnitudes $\langle V\rangle = 11.269$ mag, $\langle I\rangle = 10.441$ mag, and the variability type QPER (an SR variable with a stable period). The observations in both bands unfortunately are not simultaneous, and the behaviour of the $V - I$ colour with phase depends on the details of interpolation. Nevertheless, the $V - I$ variations did not exceed ± 0.04 mag, in agreement with the TASS observations. Using the latest data for the smallest aperture size of 30 arcsec, which is similar to ours and avoids contamination from a nearby star, we obtained the period values of 122.06 ± 0.65 d for the V band and 127.15 ± 1.06 d for the I band. One should note that the quality of the V-band measurements in the ASAS catalogue is very poor – 91 per cent of data points have the lowest grade 'D' and only 8 per cent grade 'A'. The I-band measurements are much better, with 67 per cent having grade 'A'. Hence, we adopt $P = 127.15$ d for this data set.

In Fig. 6, we show four years of *Kepler* photometry of IRAS 19135+3937 (= Kepler 4644922) carried out by the *Kepler* satellite. We plot 18 long-cadence data sets that were available in the STScI archive at the beginning of 2014. Due to the fact that the time-scale of variations exceeds the duration of a *Kepler* observing quarter, the de-trending procedure performed by the *Kepler* pipeline is invalid. Raw fluxes are therefore plotted, where small offsets between adjacent data sets result from the imperfect calibration. Applying PERIOD04 to these data, we obtain $P = 127.497 \pm 0.014$ d. The *Kepler* light curve is the most precise of all observations. It is extremely smooth and shows that the brightness variations are very regular, but the shape is not fully repeatable from cycle to cycle.

[7] http://www.astro.uni.wroc.pl/ldb/asas/kepler.html

Table 2. Summary of the photometric observations.

survey	P (d)	$\langle V\rangle$ (mag)	ΔV (mag)	$T_{\rm start}{}^a$ (d)	ΔT (d)
TASS	127.11 ± 0.95	10.69	0.9	52 782	477
ASAS	127.15 ± 1.06	11.36	0.7	53 884	598
Kepler	127.50 ± 0.01	N/A	N/A	54 953	1471
SAI	126.53 ± 0.40	11.23	1.2	56 093	519

Note. [a]First day of observation, JD−2400000.

The summary of all photometric observations (except *Tycho-2*) is given in Table 2. As can be seen, there is no indication from this data that the period changed over the past 10 years. The shape of the light curve and the mean magnitude, however, did change from cycle to cycle, confirming the SR classification of the star. In Fig. 7, we plot all observations in the V band together. *Tycho-2* measurements have been omitted from the plot due to the large error bars and the *Kepler* ones due to a non-standard pass-band. We performed a period search on this combined data set (200 data points), by preliminary scaling each of the three data sets to their average magnitude, and obtained $P = 127.04 \pm 2.6$ d, which, as will be shown in the next section, coincides with the spectroscopic period.

Our simultaneous *UBV* photometry enabled us to study colour variations in IRAS 19135+3937 for the first time. Fig. 8 shows an area on the $U - B$, $B - V$ two-colour diagram traversed by IRAS 19135+3937. The sequences of supergiants and bright giants according to Schmidt-Kaler (1982) are drawn for reference. From our spectroscopic analysis it follows that at maximum light the star should be of SpT F7 (±2). According to the supergiant calibrations of Schmidt-Kaler (1982) and Kovtyukh (2007), this corresponds to $(B - V)_0 = 0.48 \pm 0.1$ mag. The observed $(B - V)$ at maximum light is ∼0.66, hence $E(B - V) = 0.18 \pm 0.1$ mag. Assuming that this reddening is predominantly interstellar, and adopting the standard reddening law of Hiltner & Johnson (1956): $E(U - B)/E(B - V) = 0.72 + 0.05E(B - V)$,– we have de-reddened all points in Fig. 8 by this value. As can be seen, the colours vary considerably throughout the cycle, but follow neither reddening nor temperature sequences. While in the maximum light both colours can be explained by a moderately reddened F7 Ib supergiant, in the minimum light the star cannot be brought to the same locus on the *UBV*

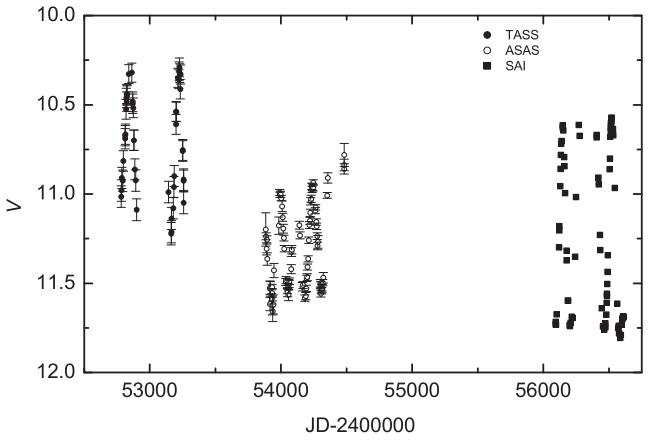

Figure 7. Combined V-band light curve based on the TASS, ASAS, and our photoelectric photometry (SAI).

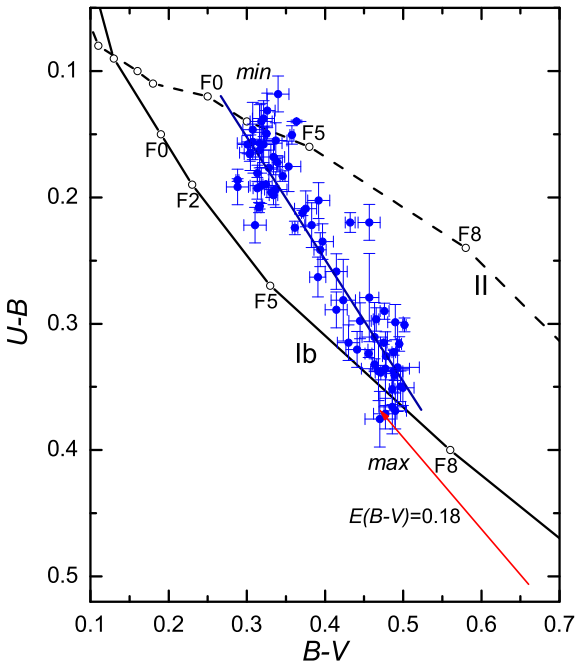

Figure 8. Location of IRAS 19135+3937 on the $U-B$ versus $B-V$ diagram, de-reddened by $E(B-V)=0.18$ and fitted with a straight line to guide the eye. The corresponding reddening vector is shown as a red line, following equation $E(U-B)/E(B-V)=0.72+0.05E(B-V)$. Black solid and dashed lines designate sequences of supergiants (Ib) and bright giants (II), respectively.

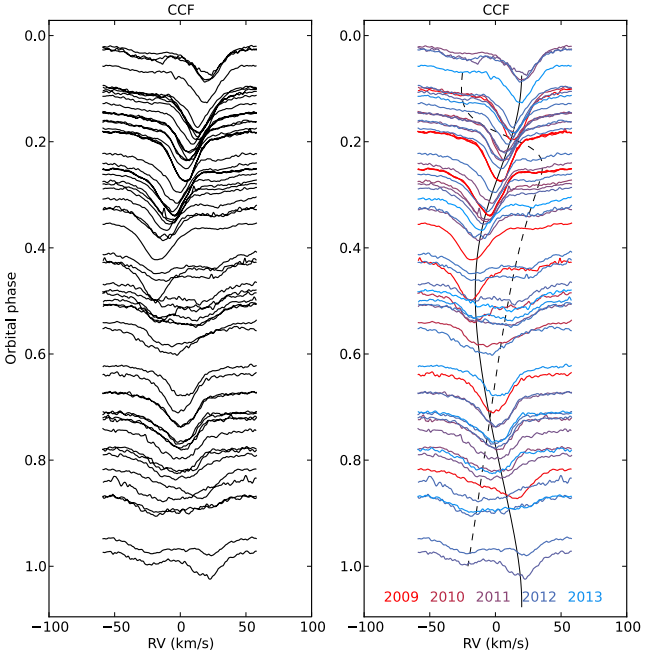

Figure 9. CCFs arranged according to the orbital phase, with time running downwards. Throughout the paper, the phases have been defined as follows: $\phi=(\mathrm{JD}-2454\,980.424\,64)/127.08$, with $\phi=0$ corresponding to $\mathrm{RV}_{\max}$. The colours on the right-hand panel designate the year of observation to illustrate the cycle-to-cycle variations. The solid and dashed lines trace the main and the secondary CCF components, respectively.

diagram even when allowing for a different amount of reddening. Pulsations can hardly explain this behaviour either, as such stars normally get redder at minimum light. Could the blue colours at minimum light be due to the contribution of an early-type companion? In the next section, we will examine our time series of spectra to investigate this possibility.

5 SPECTROSCOPIC VARIABILITY

5.1 Radial velocities

To determine RV of IRAS 19135+3937, we used a cross-correlation method with a mask containing lines of a G2 star. The correlation was performed on the order-by-order basis, after which the CCFs from the central 20 orders were merged into one to represent an average line profile. Normally, this profile would be fitted with a Gaussian to obtain an RV measurement. However, in many phases the CCFs turned out to be of a more complex shape. While some CCFs have the form of a single absorption component, either strong and narrow or shallow and broad, in other CCFs two separate components can be clearly seen. The determination of the CCF centroid is therefore not straightforward.

To investigate whether this behaviour could be periodic, we first measured a flux-averaged value of the RV for each CCF, using $(1-F_\lambda)^2$ as a weighting function. Applying PERIOD04 to these data revealed several peaks on the periodogram, of which the first two strongest ones are at 63 d and 129 d. The latter coincides with the photometric period, while the former reflects the fact that the lines split twice per photometric period. Arranging the CCFs according to the phase calculated with the longer period allowed us to identify the main component (which is usually the stronger one) and the secondary component in the split CCFs (Fig. 9). We then re-determined RVs separately for each component using a double-Gaussian fit. In several cases, it was not possible to identify the secondary component, because it was in the noise or merged with the main component. In such cases a single-Gaussian fit was performed, and the RV was assigned to the main component. The resulting RVs are given in Table A2.

In order to determine whether the main RV component could be due to the orbital motion of the brighter star (the primary) in a binary system, we fit it with a Keplerian orbit, which included a re-evaluation of the period. The fit is very good – see Table 3 and Fig. 10. The larger residuals from the fit between phases 0.4 and 0.9 are due to the broader CCFs. To estimate the uncertainties on the orbital parameters, we carried out 1000 Monte Carlo realizations to simulate the observed RVs. For each date, we used a

Table 3. Orbital elements for the primary (pAGB) component of IRAS 19135+3937.

Parameter	Value	σ
P (d)	127.08	0.08
$a\,sini$ (au)	0.20	0.007
$f(m)$ ($\mathrm{M}_\odot$)	0.07	0.007
K (km s^{-1})	17.71	0.5
e	0.14	0.02
ω ($^\circ$)	66	14
T_0 (JD)	2454 997.8	6.8
γ (km s^{-1})	1.3	0.4
χ^2_{red}	1.11	
R^2	95.4 per cent	

Note. Listed are orbital parameters with their uncertainties, reduced chi-square, and the coefficient of determination.

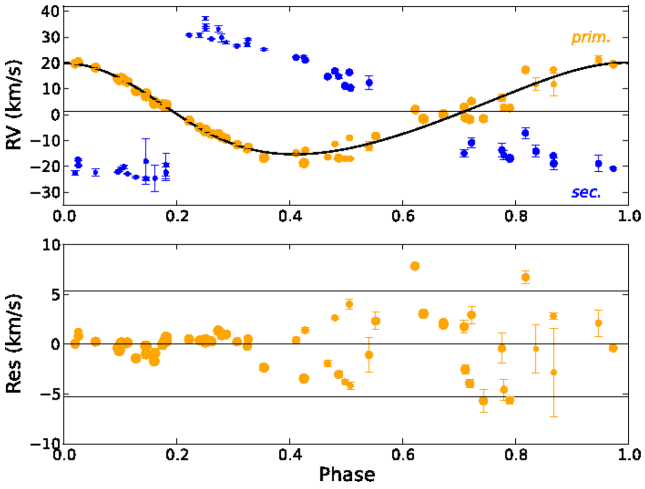

Figure 10. Radial velocities for the main component of the CCF (orange circles) and for the secondary component (blue). The former were fitted with a Keplerian orbit, which is drawn in the upper panel, while the residuals from it are plotted in the lower panel. The size of the circles is proportional to the component's strength. Horizontal lines mark $\pm 3\sigma$ deviation from the fit orbit.

Gaussian distribution centred on the observed RV and σ adopted as follows: 0.7 km s^{-1} for the orbital phases between $\phi = 0.95 - 1.35$ and 3.5 km s^{-1} for $\phi = 0.35 - 0.95$, based on the residuals from the Keplerian fit. For each realization the orbital parameters were determined, and the σ of the distribution of a given parameter was adopted as the parameter's uncertainty. Fig. 11 illustrates this procedure for the period and eccentricity.

The RV curve of the secondary CCF component is much less certain, in particularly between phases 0 and 0.3, so we did not attempt to model it. However, we can use the deduced mass function from the fit to the RV of the main component to estimate the mass

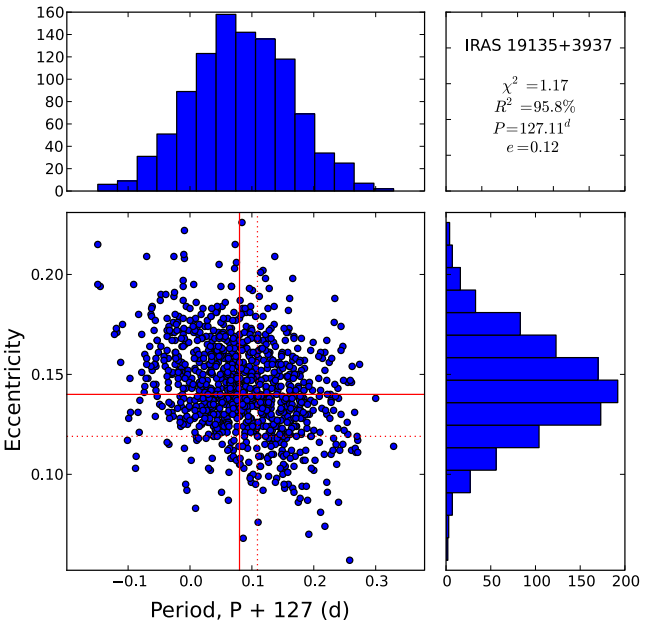

Figure 11. Distribution of values for eccentricity and orbital period based on 1000 Monte Carlo simulations of the RVs of the main CCF component. Solid lines mark a Keplerian solution obtained from the observed RVs, whereas the dotted lines denote a simulated RV set that resulted in the smallest χ^2 value.

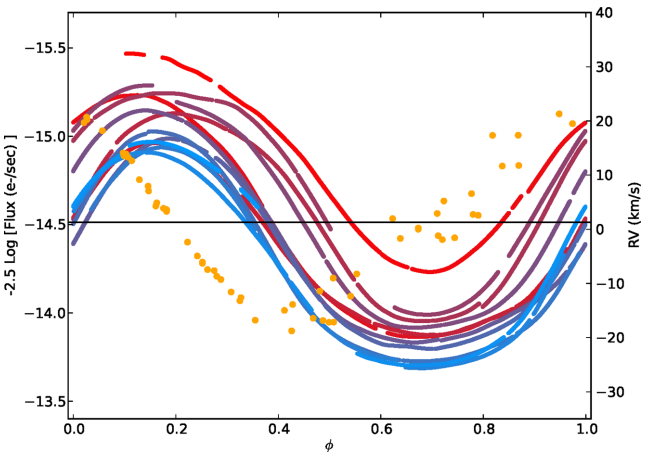

Figure 12. Radial velocities (orange circles) and *Kepler* fluxes (red to blue points) plotted against the orbital phase. The colour scheme is the same as in Figs 9 and 14. The horizontal line marks the systemic velocity.

of the putative companion. Adopting 0.5 $M_\odot$ for the mass of the pAGB primary (a mass of a typical white dwarf), with the mass function of 0.07 $M_\odot$ we obtain masses of the companion between 1.1 and 0.4 $M_\odot$, depending on the adopted inclination of 30° and >65°, respectively. The companion has a comparable or larger mass than the primary.

IRAS 19135+3937 turned out to be yet another disc system that is a binary. The line behaviour is reminiscent of the double-lined spectroscopic binaries, but not identical: the relative strengths of the two CCF components in our case vary, both with phase and from cycle to cycle. While the main component can be safely attributed to the pAGB star, the association of the secondary component with a physical companion is not straightforward.

In Fig. 12, we overlay RVs of the main CCF component and the *Kepler* photometry, that were obtained over the same time-span. Despite the cycle-to-cycle variations in the light curve, an offset of a quarter of a period can be clearly seen with the RV curve: the superior conjunction of the primary star ($\phi \sim 0.2$) coincides with the maximum light, while the inferior conjunction ($\phi \sim 0.7$) with the minimum light. Brightness declines are therefore consistent with the obscuration of the primary by the inner disc wall.

Over half of the orbit centred on the minimum light ($\phi = 0.4$–1.0) one also observes an increase in the RV scatter. As can be seen in Fig. 9, this is not due to the decreased S/N, but due to the fact that the secondary component of the CCF becomes of comparable strength to the main component, resulting in the shallower, smeared combined profiles that are difficult to fit. This is not surprising considering that at $\phi = 0.7$ the primary becomes obscured, and the spectrum of the companion should become more visible. In Section 6.3, however, we will present some arguments that hinder a definite identification of the secondary CCF component with the spectrum of the companion.

5.2 Emission lines

There are a number of variable emission lines in the spectrum of IRAS 19135+3937. Fig. 13 presents an overview of the discussed features in the form of dynamic spectra. The upper panel shows the behaviour of the photospheric lines using the example of the CCF and one strong Ba II line; the middle panel shows emission-absorption profiles of H α and one component of the NaD doublet;

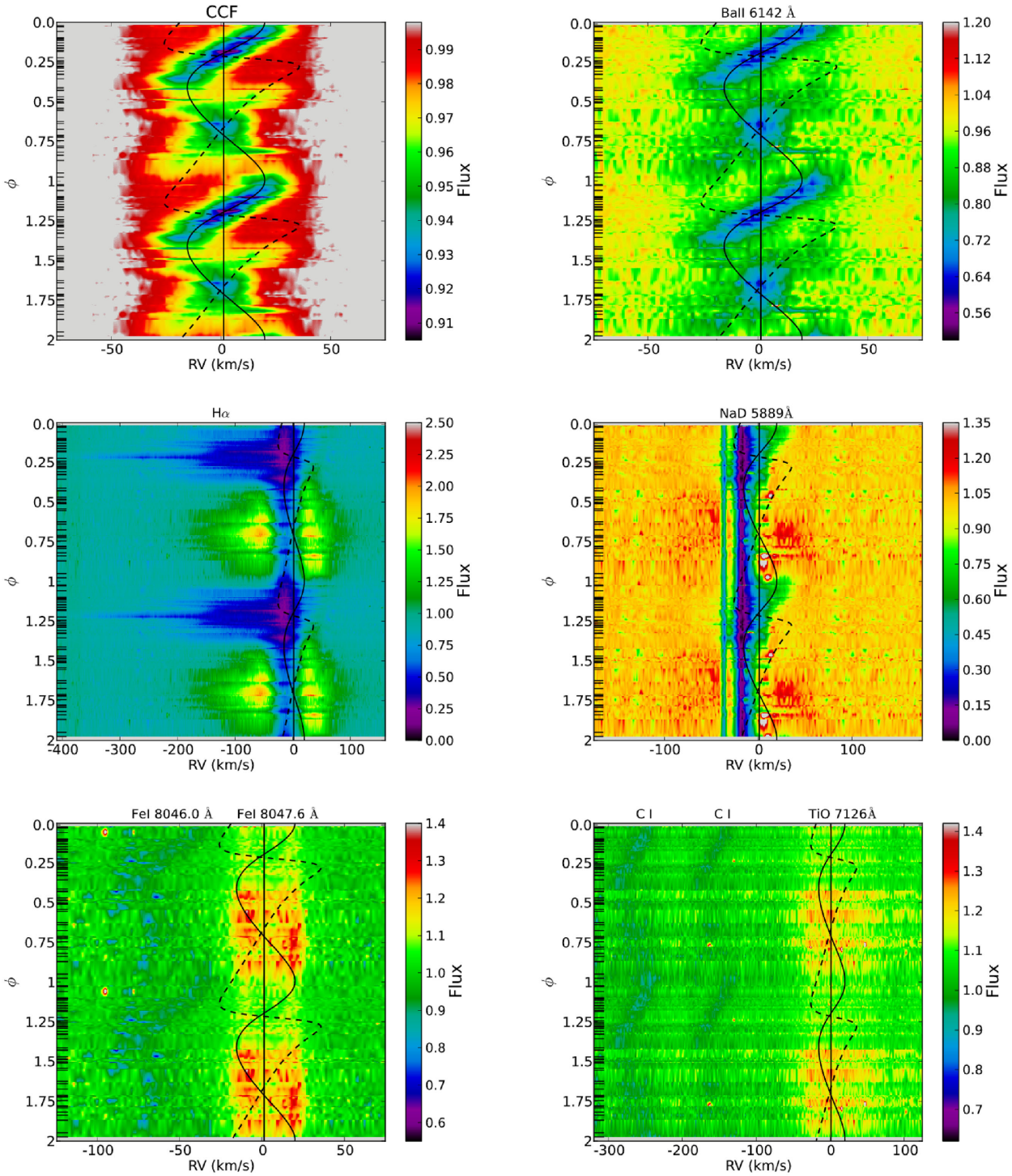

Figure 13. Dynamic spectra of the representative features in the spectra of IRAS 19135+3937: top panel shows the behaviour of the photospheric absorption lines, middle panel – lines dominated by the circumstellar emission and absorption, bottom panel – pure emission lines (with the neighbouring photospheric lines of Fe I and C I shown for reference). Colours represent continuum-normalized fluxes, with unity corresponding to the continuum level. Spectra are arranged according to the orbital phase with period 127.08 d; one period is shown twice; time runs down. The following lines are drawn to guide the eye: vertical line for the centre-of-mass velocity, solid curve – for the Kepler's solution of the main CCF component, dashed curve – of the secondary component. Short horizontal dashes designate observed phases.

the bottom panel compares static emission lines of Fe and TiO with the nearby dynamic photospheric lines.

The most prominent emission line is Hα (higher members of the Balmer series show a similar behaviour, but to a much smaller degree and confined to the line core). Hα profiles, arranged according to the orbital phase, are shown in Fig. 14. Over one-half of the period, centred on $\phi = 0.7$ (pAGB inferior conjunction), the profiles take a shape of a double-peak emission, with a distance

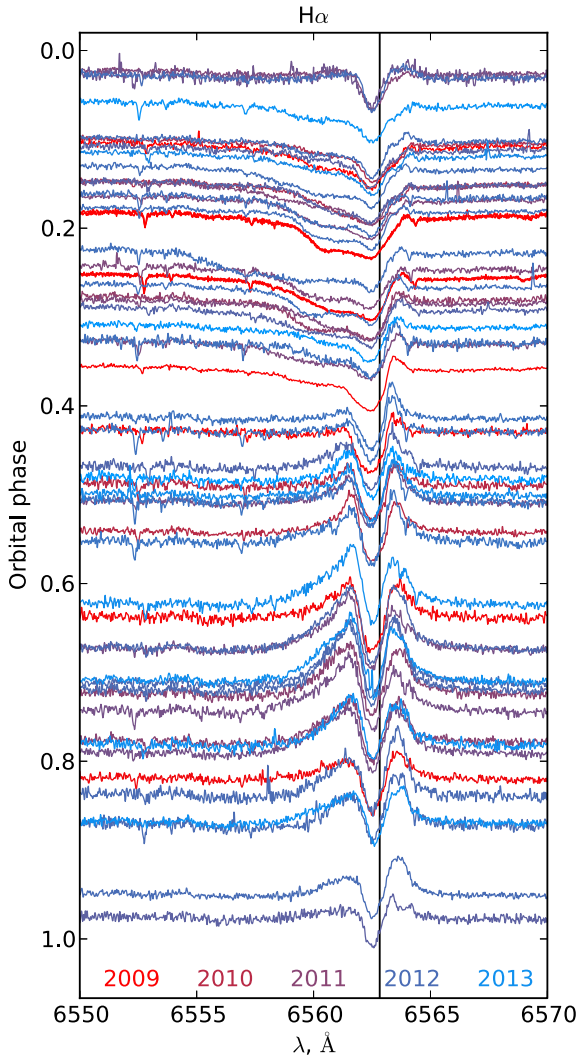

Figure 14. Hα as a function of the orbital phase. Vertical line marks the systemic velocity.

between the peaks of $\sim$100 km s^{-1} and a width at the base of at least 300 km s^{-1} (before photospheric absorption subtraction). Alternatively, such profiles can be interpreted by a broad emission profile with a narrower superimposed absorption component. This absorption cannot be photospheric due to the fact that it does not follow the orbital motion, but is permanently 13 km s^{-1} blue-shifted relative to the systemic velocity. Over another half of the period the emission in Hα is overtaken by a broader, asymmetric absorption, with a blue wing that extends to over 350 km s^{-1} near $\phi = 0.2$ (pAGB superior conjunction). This behaviour is identical to that in BD+46°442 (Gorlova et al. 2012b).

In some spectra, we also spotted weak emission in a number of low-excitation metallic and molecular lines. To study a possible correlation with the orbital phase, we first averaged spectra within each of 10 phase bins to increase the S/N. These combined spectra arranged according to the phase are shown in Fig. 15. Three examples of emission features are given: the resonance lines of Na I, low-excitation Fe I line 8047.62 Å ($\chi_{\rm low} - \chi_{\rm up} = 0.9$–$2.4$ eV), and three close TiO band-heads.

The Na D lines in IRAS 19135+3937 are dominated by a composite 'shell' absorption component, which is common for pAGB stars. The photospheric component is only visible around $\phi = 0$, when it is maximally redshifted. Throughout the rest of the orbit it is hidden in a cluster of narrow absorption lines, that are permanently blue-shifted relative to the systemic velocity. Different features can be better traced in the dynamic spectra, as shown in Fig. 13 (middle-right panel). There, the Na D photospheric absorption can be traced up to $\phi = 0.4$, which corresponds to the least obscured part of the primary's orbit, when other photospheric lines are strongest as well. At least two non-photospheric absorption components can be disentangled: at -38 and -20 km s^{-1}, that can be both of inter- and circumstellar origin. What is not so common is the appearance of the broad emission wings between $\phi = 0.6$ and 0.8 (in Fig. 13 they can be seen as a flux excess over the mean profile), that are reminiscent of emission in Hα.

Some weak emission lines are found in the red part of the spectrum, where they better stand out against the dropping continuum. The three most notable lines can be associated with two close low-excitation multiplets ($\chi_{\rm up} = 2$–3 eV) of Fe I, with rest wavelengths of 6400.32, 6498.94, and 8047.62 Å . Many more can be hidden in the telluric features and noise. Careful examination reveals that they have double-peak, but relatively narrow, profiles (the distance between the peaks is $\sim$ 30 km s^{-1}), that are permanently centred on the systemic velocity (within 3 km s^{-1}). The latter two lines were also noted by us in BD+46°442, but in the case of IRAS 19135+3937 they are stronger and clearly variable. In the continuum normalized spectra, they appear to vary in strength with the photometric/orbital period. They are 2.5 times stronger in the minimum light than in the maximum, which coincides with a one magnitude amplitude of the photometric variations. This means that the line emission flux is constant, and the apparent line variability is due to the variations in the continuum flux.

Finally, we detected weak emission from three TiO band-heads belonging to the $\gamma(0, 0)$ system. Similarly to the atomic emission lines, they become strongest during the minimum light, and appear to be stable in the RV. The individual transitions, however, are blended with each other, so it is not possible to gauge the kinematics of the emitting region.

6 DISCUSSION

We showed that IRAS 19135+3937 possesses typical characteristics of a pAGB star with a dusty disc: it is a low-gravity F star with large IR excess but low reddening, it is deficient in refractory elements, and it has a strong and variable Hα profile indicative of mass-loss. In particular, it is very similar to BD+46°442 described in our earlier work (Gorlova et al. 2012b). The only substantial difference between the two is that IRAS 19135+3937 is a recognized variable star due to the larger amplitude of the light curve. The HERMES survey uncovered periodic, but complex spectral behaviour in both stars. In the following subsections, we will elaborate upon our model of an interacting binary system that we developed for BD+46°442 to explain additional aspects exhibited by IRAS 19135+3937: brightness variations (Section 6.1), stationary emission lines (Section 6.2), photospheric line splitting and peculiar colour variations (Section 6.3).

6.1 Binarity and SRd variability

For the first time we have demonstrated that IRAS 19135+3937 is also variable in RV, with a period coinciding with the photometric period. We can now use the same argument as for BD+46°442 to disregard pulsations as the cause of variability. Integrating the RV curve of the main CCF component over half of the period, we obtain

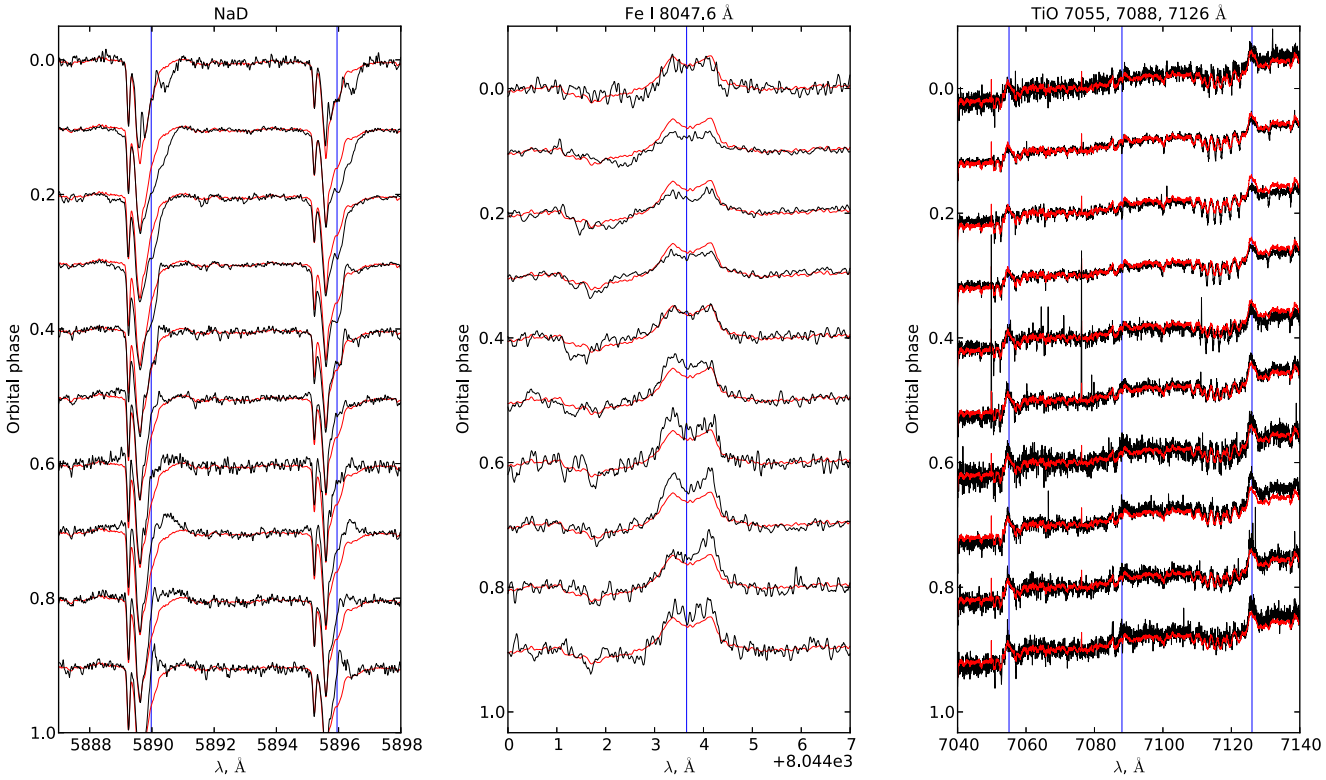

Figure 15. Emission lines as a function of orbital phase. Black: an average of all spectra falling within a given phase bin; red: an average spectrum over the entire orbit. All spectra have been normalized to unity at the continuum and shifted vertically according to the orbital phase. Vertical lines mark wavelengths for the identified features at the systemic velocity.

a displacement ∼90 $R_\odot$, which is comparable with the radius of the pAGB star itself and would be prohibitively large for pulsations. And if line splitting were due to the propagation of shock waves, as in RV Tau stars, one would have to explain why this star does not show other characteristic features of these variables, such as interchanging deep and shallow minima, and, most notably, variations in the effective temperature.

The constancy of $T_{\rm eff}$ is demonstrated in Fig. 16, where we compare a part of IRAS 19135+3937 spectrum in the phases of minimum and maximum light with the spectra of two standard F supergiants from the UVES POP archive: HD 74180 (F3 Ia; Malaroda 1975) and HD 108968 (F7 Ib/II; Houk & Cowley 1975). The standards were chosen to have SpTs expected for IRAS 19135+3937 based on its $B - V$ colour in those phases. It can be seen that in the late-F standard the lines of neutral species become noticeably stronger than in the early-F one. In the spectra of IRAS 19135+3937, however, this effect is not observed, hence, the temperature must have remained constant between the two opposite phases. Another confirmation of this fact is that Rao & Giridhar (2014) studied IRAS 19135+3937 in the intermediate phase ($\phi = 0.49$) and obtained precisely the same value of $T_{\rm eff}$ as us.

We conclude that the RV variations in IRAS 19135+3937 are due to the orbital motion of the giant primary around a much fainter companion, which is very common among pAGB stars with discs. The periodic SR dimmings can be explained by the obscuration of the primary by the circumbinary disc matter, most likely by the puffed-up inner rim during the inferior conjunction. The absence of a flat part on the light curve near maximum light could be due to the permanent obscuration or presence of a large amount of scattered light. This explanation has been already proposed for a few other long-period pAGB variables with the same phase shift between the light and RV curves, such as HR 4049

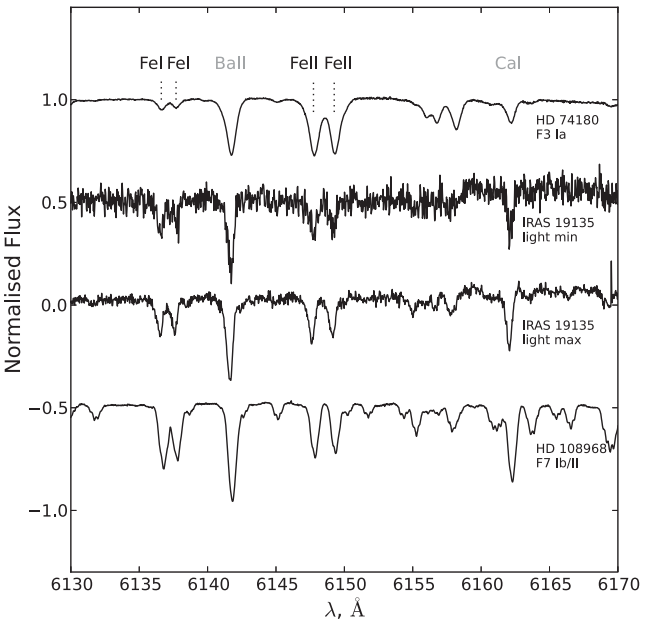

Figure 16. Comparison of IRAS 19135+3937 spectra in the phases of minimum and maximum light with each other and with two spectral standards.

(Waelkens et al. 1991), HD 52961 (Van Winckel et al. 1999), and EN TrA (Van Winckel et al. 2009). The very smooth Kepler light curve indicates that the photosphere of IRAS 19135+3937 is very stable.

6.2 Accretion on to companion and gas discs

Furthermore, a number of spectroscopic features in IRAS 19135+3937 point to the presence of an *active mass transfer* between the primary and companion. In particular, as was described in Section 5.2, near $\phi = 0.25$ Hα develops a spectacular P Cyg-like profile. With our phase convention, where phases are counted from the time of the maximum RV of the primary, $\phi = 0.25$ for a nearly circular orbit corresponds to the giant's superior conjunction (where it is farthest away from us, while the putative companion is in-between). In Gorlova et al. (2012b) and Gorlova et al. (2013), we describe a few other systems from the HERMES survey and from the literature with a similar behaviour of Hα. As was shown by Thomas et al. (2013) for the central star of the RR nebula, this phenomenon can be explained by a wide-angle jet originating at the secondary. The lobe pointing in our direction will be periodically projected against the giant primary and produce the observed transient blue-shifted absorption. The jet is likely powered by accretion from the pAGB primary to the secondary.

The interpretation of the double-peaked emission lines is not so straightforward. Using STIS spectrograph on the *Hubble Space Telescope*, Thomas et al. (2011) spatially resolved narrow emission (with the distance between the peaks of 12 km s^{-1}) in the NaD lines of the RR, and deduced that it is produced in the distant parts of a bipolar outflow, that are seen in the direct light. On the other hand, the much broader emission in Hα according to Witt et al. (2009) could form in the parts of the lobes that are closer to the binary. The RR, however, is not a typical disc object, and the appearance of some features may be affected by its nearly perfect edge-on orientation.

In Fig. 17, we show another possibility to explain the formation of the double-peaked emission profiles – in a Keplerian disc. Smak

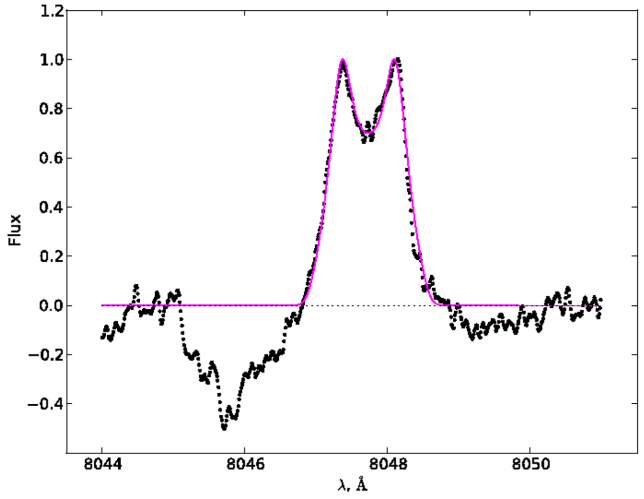

Figure 17. Mean, continuum-subtracted observed profile of an Fe emission line in IRAS 19135+3937 (dots) versus the best-fitting model profile from a Keplerian disc (solid). Both profiles have been normalized to unity at maximum flux. The broad absorption feature in the observed spectrum is due to the averaging of a neighbouring photospheric line over the entire orbit.

(1969) presented a simple kinematic model of purely gaseous, optically thin disc of constant thickness with density linearly dropping to zero at the outer edge. Using this formulation, we could successfully fit Fe emission line profiles in IRAS 19135+3937 with the following disc parameters: the ratio of the inner to outer radius of 0.15, and the velocity at the outer edge of 12 km s^{-1}. Depending on the total mass of the system (0.9–1.6 M$_\odot$) and the inclination angle (30–70°), this results in a disc with $R_{\rm in} = 0.2$–1.3 au and $R_{\rm out} = 1.4$–8.7 au.

Is this Fe disc circumcompanion or circumbinary? In Section 5.1, we deduced that the semi-major axis of the pAGB primary is 0.2–0.4 au and the secondary is likely more massive than the primary. Hence, the distance between the companions does not exceed 0.4–0.8 au, which is smaller than the outer radius of the Fe disc. This fact, together with the constancy of the RV of the emission lines, implies that this disc is *circumbinary*. Furthermore, when applying a 2D radiative transfer code (Gielen et al. 2007, 2009) to fit the SED of IRAS 19135+3937, we obtain that the inner radius of the circumbinary *dusty* disc is 5–10 au. Thus, the double-peaked Fe emission lines may signal the presence of a gaseous Keplerian circumbinary disc, that is nestled within the sublimation boundary of the dusty disc.

In the prototypical disc object 89 Her the above discussed metal lines form part of a much richer emission line spectrum (Climenhaga et al. 1987; Kipper 2011). Based on the constancy of the RV, Waters et al. (1993) were first to propose that emission could originate in a circumbinary disc. Indeed, Bujarrabal et al. (2007) possibly detected such a disc as an unresolved component in the interferometric maps of CO. The existence of gas inside a dusty disc has been long anticipated in the framework of the re-accretion hypothesis, designed to explain a depletion pattern in some disc hosts. The observational evidence of circumbinary gas, however, is largely missing. CO studies normally probe material on a much larger scale (10^3–10^5 au; Bujarrabal et al. 2013), which could have been ejected in the preceding AGB stage. In contrast, metal emission lines probe gas on au scales, and therefore provide a better insight into the current mass-loss/accretion.

Furthermore, the ∼10 times wider emission in Hα may indicate the presence of gas well inside the binary's orbit. Giving that there is a jet emanating from the companion, this hot gas could form in the *circumcompanion* accretion disc. Interestingly, the rare appearance of TiO in emission has been also associated with the presence of an accretion disc. Thus, Hillenbrand et al. (2012) proposed to explain TiO emission in some young stellar objects (YSOs) and Be stars by evaporating disc material at the base of the outflow, where it is lifted up and exposed to the UV radiation from the accretion disc. Besides IRAS 19135+3937, TiO emission has been recently discovered in a few candidate pAGB binaries in the Magellanic Clouds (Wood, Kamath & Van Winckel 2013).

This raises some important questions about the type of the accretion (a wind, a Roche lobe one, or perhaps even accretion from the circumbinary disc), and whether the three discs (the circumcompanion, circumbinary, and the outer dust+gas one) could be possibly related to each other. The exploration of these possibilities, however, is beyond the scope of this paper.

6.3 Reflection of the circumbinary disc

What is the nature of the companion and could it explain the remaining peculiarities of the system: the secondary set of spectral lines and the blueing of the colours in the light minima?

We applied the FDBINARY code[8] (Ilijic et al. 2004) to our spectral data set in the attempt to separate the two components. The code performs separation of spectra in a spectroscopic double-lined binary star in Fourier space without the use of template spectra. The input consists of the continuum-normalized spectra, the relative fluxes of the two components ('light factors') per observation, that were taken from our double-Gaussian decomposition of the CCFs, and the first approximation for the orbital parameters. In the output, we obtained two identical sets of lines, whose shape and relative depths depended somewhat on the selected regions and the number of iterations, but in no case was there an indication that the sets would correspond to two different SpTs. This fact, along with the constancy of temperature in the opposite conjunctions, implies that the companion must have an identical SpT and comparable luminosity to the primary. And yet, only one star is seen in the light curve (no substantial secondary minimum/maximum is observed over the RV period). Also from the evolutionary point of view it is very unlikely to find a system composed of two yellow evolved stars, as pAGB stage is extremely short (∼1000 yr).

To resolve these difficulties, we propose an alternative explanation for the secondary component of spectral lines, in IRAS 19135+3937, BD+46°442, RR and potentially other inclined disc systems with periodically distorted lines. In this picture the companion is undetected, probably a non-evolved dim MS star. The secondary set of lines, which is most pronounced near the inferior conjunction of the primary, would be the light of the primary that is reflected off the inner wall of the disc and scattered into our line of sight. The reflected image will move in the opposite direction from the star and disappear during the superior conjunction of the latter, explaining the CCF behaviour.

A very similar phenomenon of line splitting due to the presence of reflected light was described for one classical T Tauri binary KH 15D (Herbst et al. 2008). Similar to IRAS 19135+3937, KH 15D experiences periodic SR deep declines, that are explained by the orbital motion inside a precessing warped disc (Herbst et al. 2010; Windemuth & Herbst 2014). The SEDs of pre-main-sequence objects are often indistinguishable from the pAGB ones, pointing to the similarity of their discs (de Ruyter et al. 2006). One such property is the presence of grains that are larger than in the interstellar medium. Based on the comprehensive modelling, Herbst et al. (2008) concluded that the reflected light in KH 15D provides the best evidence that the particles in the disc grew to at least 1 mm in size. For pAGB discs the same was previously inferred from the blackbody slope of the far-IR excess, which can only be measured for brighter sources. Modelling of the scattered line profiles may prove to be a useful novel tool for studying composition and kinematics of post-AGB discs (e.g. Grinin, Mitskevich & Tambovtseva 2006). While in YSOs the particle growth is the first step towards the planet formation process, the evolution of grains in post-AGB discs is unknown.

Large particles, however, produce grey scattering and settle to the mid-plane of the disc, and hence cannot explain the blueing of the system in the minimum light when the primary sinks behind the disc edge. No trace of a hot companion is observed in our spectra either. We propose that the blueing is due to the scattering by the inner wall of the disc. Since we do not resolve the system, the total flux in the telescope beam is always a sum of direct and scattered light in our line of sight. During the inferior conjunction of the primary (phase of minimum light) the amount of bluer, back-scattered (by the farthest side of the inner disc wall) light may exceed the amount of direct, reddened light from the primary, which is possible because, unlike us, the inner disc wall always sees the star unobscured. As a result, in this phase the system will appear bluer to us than in the unobscured phases.

The colours and the level of the scattered light bring stringent constraints on the size distribution and on the chemo-physical properties of the dust grains, as well as on geometry of the inner dusty disc. The reproduction of these observables will need detailed radiative transfer models in which the angle and colour-dependent scattering, as well as dust settling need to be incorporated. This is outside the scope of this paper, however, and will be the subject of a subsequent analysis. The high level of optical scattering seems to be a common property of the circumbinary discs, as also in 89 Her this has been detected using optical interferometry. Hillen et al. (2013, 2014) spatially resolved the optical scattering component and deduced that as much as 40 per cent of the optical flux of 89 Her is due to scattered light.

6.4 Circumstellar geometry

In Fig. 18, we present an artist's impression of the circumstellar environment of IRAS 19135+3937 based on the discussion in the previous subsections. Like in BD+46°442, in this system the giant primary is transferring mass to a, likely unevolved, companion, which results in the production of a pair of jets emanating from the secondary. The system is surrounded by a dusty disc, and possibly also a smaller gaseous disc. The new element in this picture is the high level of optical reflection from the primary on the wall of the circumbinary disc, that mimics a twin companion in the spectra. This reflected light is observed with a different Doppler shift and hence can be differentiated from the component of direct light. The reflected spectrum and the light amplitude are more pronounced in IRAS 19135+3937 than in BD+46°442 likely due to the higher inclination of the former. The contribution of this reflected light is maximal at minimum light, which indicates an efficient back-scattering and makes the system to appear bluer when fainter.

7 CONCLUSIONS

We presented contemporaneous photometric and spectroscopic observations of IRAS 19135+3937, an SRd variable with an IR excess. It is often assumed that variability of such stars is due to pulsations, but there is no theoretical study yet that would consistently reproduce all types of SR variables. We showed that IRAS 19135+3937 is a binary system with a circumbinary dusty disc. These two properties, taken together, can explain the observed light variations with a period of 127 d by an obscuration of the primary star by the inner edge of the disc during inferior conjunctions. Given the very smooth Kepler light curve, the photosphere of IRAS 19135+3937 is stable and does not show any pulsations.

IRAS 19135+3937 presents a typical case of a class of pAGB binaries where circumstellar matter is confined to a disc: it is a low-gravity object, a single-line spectroscopic binary, shows a depletion pattern of the refractory elements (albeit on a weaker side of the range), and has a jet-like outflow from the companion, based on the specific Hα profiles. The commonality of the latter phenomenon was realized thanks to the HERMES survey (Gorlova et al. 2013). Furthermore, we detected static emission lines of Fe I and TiO that are most pronounced in the spectra taken near minimum light. We successfully fit the double-peaked Fe lines with a circumbinary

[8] http://sail.zpf.fer.hr/fdbinary

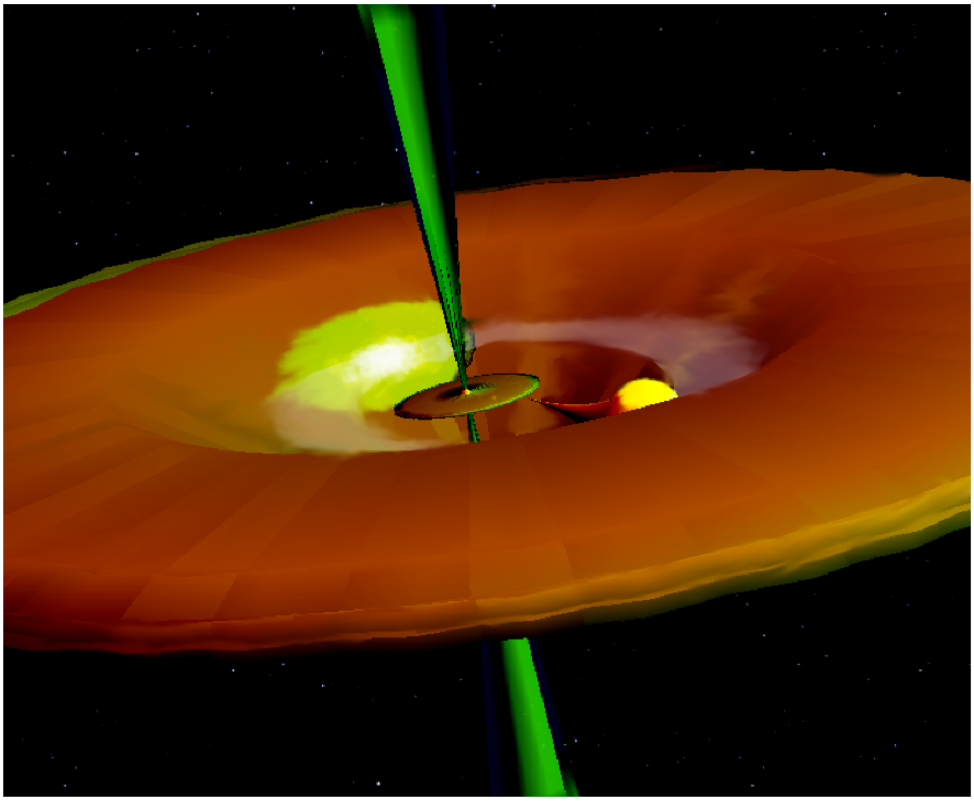

Figure 18. Artist's impression of IRAS 19135+3937 interacting binary system, depicted in the phase near light minimum. The pAGB primary is about to sink behind the dusty disc edge, giving way to the spot of reflected light on the opposite side of the circumbinary disc.

Keplerian disc, that may be the first evidence of the star–disc interaction leading to the depletion pattern in pAGB atmospheres. The nature of the invisible companion remains unknown. We detected a secondary set of spectral lines, but prove that it must be a reflected spectrum of the primary on the disc grains, rather than a spectrum of a physical companion.

The single case of IRAS 19135+3937 presented here cannot rule out pulsations for all SRd variables. What our study illustrates is that the presence of a circumbinary dusty disc may have profound effects on the light and RV curves, and therefore needs to be considered on a par with the more traditional factors, such as stellar eclipses and pulsations.

ACKNOWLEDGEMENTS

We would like to thank Drs P. Harmanec and H. Hensberge for the fruitful discussions, the numerous observers from the HERMES consortium institutions for collecting the spectral data, and the anonymous referee for the comments that helped to sharpen the text. This study is based on observations made with the Mercator Telescope, operated on the island of La Palma by the Flemish Community, at the Spanish Observatorio del Roque de los Muchachos of the Instituto de Astrofisica de Canarias; and with the HERMES spectrograph, which is supported by the Fund for Scientific Research of Flanders (FWO), Belgium, the Research Council of K.U.Leuven, Belgium, the Fonds National de la Recherche Scientifique (F.R.S.-FNRS), Belgium, the Royal Observatory of Belgium, the Observatoire de Geneve, Switzerland and the Thüringer Landessternwarte Tautenburg, Germany.

REFERENCES

Bagnulo S., Jehin E., Ledoux C., Cabanac R., Melo C., Gilmozzi R., ESO Paranal Science Operations Team, 2003, The Messenger, 114, 10
Bessell M. S., 2000, PASP, 112, 961
Britavskiy N. E., Andrievsky S. M., Tsymbal V. V., Korotin S. A., Martin P., Andrievska A. S., 2012, A&A, 542, A104
Buchler J. R., Kovacs G., 1987, ApJ, 320, L57
Bujarrabal V., Van Winckel H., Neri R., Alcolea J., Castro-Carrizo A., Deroo P., 2007, A&A, 468, L45
Bujarrabal V., Alcolea J., Van Winckel H., Santander-García M., Castro-Carrizo A., 2013, A&A, 557, A104
Buscombe W., Foster B. E., 1995, MK spectral classifications. Twelfth general catalogue, Epoch 2000 Including UBV Photometry, Northwestern University, Evanston, Illinois, USA
Cardelli J. A., Clayton G. C., Mathis J. S., 1989, ApJ, 345, 245
Castelli F., Kurucz R. L., 2003, in N. Piskunov W. W. W., Gray D. F., eds, Proc. IAU Symp. 210, Modelling of Stellar Atmospheres. Astron. Soc. Pac., San Francisco, p. 20
Climenhaga J. L., Smoliński J., Krempeć-Krygier J., Krygier B., Krawczyk S., 1987, in Appenzeller I., Jordan C., eds, Proc. IAU Symp. 122, Circumstellar Matter. Reidel, Dordrecht. p. 329
Coelho P., Barbuy B., Melendez J., Schiavon R. P., Castilho B. V., 2005, A&A, 443, 735
De Ruyter S., Van Winckel H., Dominik C., Waters L. B. F. M., Dejonghe H., 2005, A&A, 435, 161
de Ruyter S., Van Winckel H., Maas T., Lloyd Evans T., Waters L. B. F. M., Dejonghe H., 2006, A&A, 448, 641
Deroo P., Acke B., Verhoelst T., Dominik C., Tatulli E., Van Winckel H., 2007, A&A, 474, L45
Droege T. F., Richmond M. W., Sallman M. P., Creager R. P., 2006, PASP, 118, 1666
Evans T. L., 1985, MNRAS, 217, 493

Fokin A. B., 1994, A&A, 292, 133
Gielen C., van Winckel H., Waters L. B. F. M., Min M., Dominik C., 2007, A&A, 475, 629
Gielen C. et al., 2009, A&A, 508, 1391
Giridhar S., Lambert D. L., Gonzalez G., 2000, PASP, 112, 1559
Gorlova N., 2011, J. Phys. Conf. Ser., 328, 012008
Gorlova N., Van Winckel H., Jorissen A., Van Eck S., Dermine T., Exter K., Østensen R. H., Van de Steene G., 2011, in Zijlstra A. A., Lykou F., McDonald I., Lagadec E., eds, APN 5 Conf., HERMES Survey of Binarity in Evolved Stars. Ebrary, CA, USA, p. 246
Gorlova N., Van Winckel H., Jorissen A., 2012a, Balt. Astron., 21, 165
Gorlova N. et al., 2012b, A&A, 542, A27
Gorlova N., Van Winckel H., Vos J., Østensen R. H., Jorissen A., Van Eck S., Ikonnikova N., 2013, in Pavlovski K., Tkachenko A., Torres G., eds, EAS Publ. Ser. Vol. 64, Monitoring Evolved Stars for Binarity With the Hermes Spectrograph. EDP Sciences, Les Ullis, p. 163
Grinin V. P., Mitskevich A. S., Tambovtseva L. V., 2006, Astron. Lett., 32, 110
Herbst W., Hamilton C. M., Leduc K., Winn J. N., Johns-Krull C. M., Mundt R., Ibrahimov M., 2008, Nature, 452, 194
Herbst W., LeDuc K., Hamilton C. M., Winn J. N., Ibrahimov M., Mundt R., Johns-Krull C. M., 2010, AJ, 140, 2025
Hillen M. et al., 2013, A&A, 559, A111
Hillen M. et al., 2014, A&A, 568, 12
Hillenbrand L. A., Knapp G. R., Padgett D. L., Rebull L. M., McGehee P. M., 2012, AJ, 143, 37
Hiltner W. A., Johnson H. L., 1956, ApJ, 124, 367
Houk N., Cowley A. P., 1975, University of Michigan Catalogue of Two-dimensional Spectral Types for the HD stars. Volume I. Declinations −90 to −53 deg. Univ. Michigan, Ann Arbor, MI
Høg E. et al., 2000, A&A, 355, L27
Ilijic S., Hensberge H., Pavlovski K., Freyhammer L. M., 2004, in Hilditch R. W., Hensberge H., Pavlovski K., eds, ASP Conf. Ser. Vol. 318, Spectroscopically and Spatially Resolving the Components of the Close Binary Stars. Astron. Soc. Pac., San Francisco, p. 111
Kamath D., Wood P. R., Van Winckel H., 2014, MNRAS, 439, 2211
Kazarovets E. V., Samus N. N., Durlevich O. V., Kireeva N. N., Pastukhova E. N., 2013, Inf. Bull. Var. Stars, 6052, 1
Kharchenko N. V., Roeser S., 2009, VizieR Online Data Catalog, 1280, 0
Kipper T., 2011, Balt. Astron., 20, 65
Kiss L. L., Derekas A., Szabó G. M., Bedding T. R., Szabados L., 2007, MNRAS, 375, 1338
Kovtyukh V. V., 2007, MNRAS, 378, 617
Kovtyukh V. V., Andrievsky S. M., 1999, A&A, 351, 597
Lenz P., Breger M., 2005, Commun. Asteroseismol., 146, 53
Lloyd Evans T., 1974, MNRAS, 167, 17p
Lobel A., 2008, J. Phys. Conf. Ser., 130, 012015
Lobel A., 2011, Can. J. Phys., 89, 395
Lyutyj V. M., 1971, Soobshch. Gos. Astron. Inst., 172, 30
Malaroda S., 1975, AJ, 80, 637
Mermilliod J. C., 1986, Bull. Inf. Cent. Donnees Stellaires, 31, 175
Munari U., Castelli F., 2000, A&AS, 141, 141
O'Donnell J. E., 1994, ApJ, 422, 158
Pigulski A., Pojmański G., Pilecki B., Szczygieł D. M., 2009, Acta Astron., 59, 33
Pollard K. R., Cottrell P. L., Lawson W. A., Albrow M. D., Tobin W., 1997, MNRAS, 286, 1
Rao S. S., Giridhar S., 2014, Rev. Mex. Astron. Astrofis., 50, 49
Raskin G. et al., 2011, A&A, 526, A69
Sallman M., Droege T., 2004, Inf. Bull. Var. Stars, 5600, 27
Schmidt-Kaler T., 1982, in Schaifers K., Voigt H.-H., eds, Landolt-BÃűrnstein New Series Vol. 2b, Stars and Star Clusters. Springer, Berlin
Smak J., 1969, Acta Astron., 19, 155
Sneden C. A., 1973, PhD thesis, Univ. Texas
Thévenin F., 1989, A&AS, 77, 137
Thévenin F., 1990, A&AS, 82, 179
Thomas J. D. et al., 2011, MNRAS, 417, 2860
Thomas J. D., Witt A. N., Aufdenberg J. P., Bjorkman J. E., Dahlstrom J. A., Hobbs L. M., York D. G., 2013, MNRAS, 430, 1230
Van Winckel H., 2003, ARA&A, 41, 391
Van Winckel H., Reyniers M., 2000, A&A, 354, 135
Van Winckel H., Waelkens C., Fernie J. D., Waters L. B. F. M., 1999, A&A, 343, 202
Van Winckel H. et al., 2009, A&A, 505, 1221
Van Winckel H. et al., 2010, Mem. Soc. Astron. Ital., 81, 1022
Van Winckel H., Hrivnak B. J., Gorlova N., Gielen C., Lu W., 2012, A&A, 542, A53
Waelkens C., Waters L. B. F. M., 1993, in Sasselov D. D., ed., ASP Conf. Ser. Vol. 45, Luminous High-Latitude Stars. Astron. Soc. Pac., San Francisco, p. 219
Waelkens C., Lamers H. J. G. L. M., Waters L. B. F. M., Rufener F., Trams N. R., Le Bertre T., Ferlet R., Vidal-Madjar A., 1991, A&A, 242, 433
Wahlgren G. M., 1993, in Sasselov D. D., ed., ASP Conf. Ser. Vol. 45, Luminous High-Latitude Stars. Astron. Soc. Pac., San Francisco, p. 270
Wallerstein G., 2002, PASP, 114, 689
Waters L. B. F. M., Waelkens C., Mayor M., Trams N. R., 1993, A&A, 269, 242
Windemuth D., Herbst W., 2014, AJ, 147, 9
Witt A. N., Vijh U. P., Hobbs L. M., Aufdenberg J. P., Thorburn J. A., York D. G., 2009, ApJ, 693, 1946
Wood P. R. et al., 1999, in Le Bertre T., Lebre A., Waelkens C., eds, Proc. IAU Symp. 191, Asymptotic Giant Branch Stars. Astron. Soc. Pac., San Francisco, p. 151
Wood P. R., Kamath D., Van Winckel H., 2013, MNRAS, 435, 355

APPENDIX A: NEW MEASUREMENTS OF IRAS 19135+3937

Table A1. *UBV* photometry in 2012–2013.

JD	*V*	*B*	*U*	*B* − *V*	*U* − *B*
2456 093.447	11.730	12.231	12.521	0.501	0.290
2456 094.482	11.716	12.236	12.485	0.520	0.249
2456 095.375	11.731	12.199	12.522	0.468	0.323
2456 101.456	11.674	12.158	12.454	0.484	0.296
2456 119.425	11.299	11.854	12.194	0.555	0.340
2456 121.473	11.204	11.781	12.147	0.577	0.366
2456 122.437	11.180	11.752	12.086	0.572	0.334
2456 128.378	10.955	11.550	11.940	0.595	0.390
2456 131.353	10.859	11.454	11.874	0.595	0.420
2456 133.355	10.781	11.402	11.854	0.621	0.452
2456 136.312	10.719	11.344	11.773	0.625	0.429
2456 137.447	10.702	11.312	11.758	0.610	0.446
2456 146.374	10.615	11.263	11.732	0.648	0.469
2456 147.382	10.628	11.286	11.743	0.658	0.457
2456 151.353	10.644	11.295	11.765	0.651	0.470
2456 159.404	10.793	11.448	11.895	0.655	0.447
2456 161.360	10.844	11.488	11.951	0.644	0.463
2456 166.472	10.996	11.600	12.012	0.604	0.412
2456 176.375	11.318	11.881	12.234	0.563	0.353
2456 177.302	11.372	11.913	12.269	0.541	0.356
2456 186.302	11.597	12.103	12.365	0.506	0.262
2456 189.333	11.598	12.094	12.382	0.496	0.288
2456 200.264	11.734	12.215	12.504	0.481	0.289
2456 202.319	11.740	12.233	12.545	0.493	0.312
2456 208.313	11.722	12.210	12.487	0.488	0.277
2456 216.232	11.687	12.180	12.504	0.493	0.324
2456 224.236	11.695	12.163	12.481	0.468	0.318
2456 241.222	11.352	11.878	12.192	0.526	0.314
2456 249.208	11.017	11.591	11.964	0.574	0.373
2456 270.188	10.613	11.249	11.660	0.636	0.411
2456 276.184	10.674	11.318	11.760	0.644	0.442
2456 405.565	10.669	11.349	11.831	0.680	0.482
2456 406.512	10.682	11.352	11.852	0.670	0.500
2456 420.503	10.908	11.577	12.045	0.669	0.468
2456 422.506	10.945	11.627	12.059	0.682	0.432
2456 431.517	11.229	11.865	12.216	0.636	0.351
2456 434.490	11.315	11.927	12.278	0.612	0.351
2456 445.479	11.641	12.184	12.455	0.543	0.271
2456 454.514	11.743	12.239	12.577	0.496	0.338
2456 463.510	11.760	12.265	12.546	0.505	0.281
2456 472.379	11.748	12.231	12.528	0.483	0.297
2456 473.392	11.725	12.240	12.547	0.515	0.307
2456 479.367	11.676	12.171	12.510	0.495	0.339
2456 482.428	11.609	12.113	12.434	0.504	0.321
2456 484.401	11.568	12.102	12.409	0.534	0.307
2456 485.356	11.558	12.072	12.402	0.514	0.330
2456 487.401	11.504	12.042	12.324	0.538	0.282
2456 489.405	11.437	11.988	12.332	0.551	0.344
2456 492.399	11.343	11.914	12.309	0.571	0.395
2456 504.440	10.860	11.506	11.933	0.646	0.427
2456 506.431	10.801	11.437	11.891	0.636	0.454
2456 510.426	10.679	11.347	11.801	0.668	0.454
2456 513.336	10.649	11.306	11.773	0.657	0.467
2456 513.413	10.637	11.307	11.737	0.670	0.430
2456 514.339	10.627	11.284	11.787	0.657	0.503
2456 515.397	10.606	11.279	11.744	0.673	0.465
2456 517.412	10.594	11.244	11.751	0.650	0.507
2456 518.358	10.592	11.258	11.755	0.666	0.497
2456 519.424	10.572	11.248	11.729	0.676	0.481
2456 520.379	10.575	11.249	11.697	0.674	0.448
2456 531.380	10.635	11.304	11.776	0.669	0.472
2456 533.410	10.670	11.336	11.819	0.666	0.483
2456 545.372	10.965	11.621	12.043	0.656	0.422
2456 563.302	11.615	12.127	12.454	0.512	0.327
2456 573.270	11.749	12.248	12.519	0.499	0.271
2456 574.326	11.738	12.240	12.508	0.502	0.268
2456 577.271	11.781	12.280	12.602	0.499	0.322
2456 586.236	11.807	12.324	12.649	0.517	0.325
2456 591.264	11.790	12.304	12.603	0.514	0.299
2456 597.284	11.731	12.222	12.575	0.491	0.353
2456 602.292	11.702	12.219	12.505	0.517	0.286
2456 606.257	11.687	12.183	12.477	0.496	0.294
2456 607.236	11.695	12.203	12.510	0.508	0.307
2456 612.229	11.688	12.176	12.463	0.488	0.287

Table A1 – *continued*

Table A2. Radial velocities in 2009–2013.

JD (d)	RV_{main} (km s^{-1})	RV_{sec} (km s^{-1})
2454 993.459 06	13.90	− 20.90
2455 003.509 20	3.29	− 22.24
2455 003.528 30	3.53	− 22.56
2455 003.547 40	3.62	− 19.50
2455 012.407 89	− 6.29	37.08
2455 012.427 23	− 6.05	33.09
2455 012.446 60	− 6.23	34.26
2455 025.567 87	− 16.78	25.22
2455 034.559 47	− 18.74	22.30
2455 061.444 61	− 1.69	N/A
2455 084.425 00	17.32	− 7.19
2455 423.611 70	− 16.83	14.74
2455 430.457 50	− 12.33	12.36
2455 501.335 56	13.52	− 21.61
2455 507.329 11	7.97	− 18.11
2455 650.711 84	− 7.63	33.15
2455 707.666 32	5.21	− 10.86
2455 714.509 39	6.58	− 13.75
2455 745.568 24	19.68	− 22.63
2455 761.547 27	7.06	− 24.93
2455 763.568 35	4.86	− 24.68
2455 773.618 64	− 4.93	30.83
2455 778.543 34	− 8.67	29.72
2455 784.490 19	− 12.61	29.06
2455 807.493 37	− 17.13	10.34
2455 828.428 79	0.22	N/A
2455 837.440 68	− 1.57	N/A
2455 843.359 22	2.57	− 16.91
2455 873.343 16	20.68	− 17.48
2455 993.734 19	19.49	− 20.90
2456 010.709 72	13.30	− 20.14
2456 015.643 42	7.94	− 24.72
2456 033.670 80	− 9.28	27.91
2456 056.544 96	− 16.41	14.72
2456 082.596 48	0.01	N/A
2456 087.523 59	− 1.19	N/A
2456 088.539 41	− 1.90	N/A
2456 103.405 44	11.66	− 14.23
2456 107.434 56	11.77	− 18.93
2456 117.485 52	21.29	− 18.95
2456 127.545 49	20.26	− 19.66
2456 136.417 71	14.06	− 22.11
2456 140.505 15	9.14	− 24.19
2456 144.619 82	4.28	N/A

Table A2 – *continued*

JD (d)	RV_{main} (km s^{-1})	RV_{sec} (km s^{-1})
2456 146.484 06	3.85	N/A
2456 152.458 58	– 2.36	30.74
2456 157.499 63	– 7.44	29.25
2456 165.486 63	– 13.20	27.11
2456 176.533 46	– 14.96	22.14
2456 178.584 60	– 13.87	21.02
2456 188.514 69	– 9.01	16.36
2456 194.445 81	– 8.25	N/A
2456 392.747 29	12.65	– 22.95
2456 441.692 57	– 17.15	11.11
2456 457.457 02	1.96	N/A
2456 468.488 79	2.90	– 14.97
2456 477.439 36	2.73	– 15.64
2456 488.566 07	17.36	– 15.94
2456 512.623 42	18.19	– 22.41
2456 544.466 48	– 11.58	26.57
2456 566.492 03	– 11.40	16.88

Note. HERMES radial velocities for the main and secondary components in the CCF of IRAS 19135+3937, as described in Section 5.1. 'N/A' stands for 'not available' and designates phases where it was not possible to disentangle the secondary component.

This paper has been typeset from a TEX/LATEX file prepared by the author.